

February 25, 2014

Nanostructuring of Biosensing Electrodes with Nanodiamonds for Antibody Immobilization

Wenli Zhang

Kush Patel

Andrew Schexnider

Shirin Banu

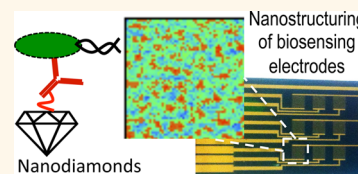
Adarsh D. Radadia, *Louisiana Tech University*

Nanostructuring of Biosensing Electrodes with Nanodiamonds for Antibody Immobilization

Wenli Zhang,[†] Kush Patel,[†] Andrew Schexnider, Shirin Banu, and Adarsh D. Radadia*

Institute for Micromanufacturing, Center for Biomedical Engineering and Rehabilitation Services, Louisiana Tech University, Ruston, Louisiana 71272, United States. [†]W.Z. and K.P. contributed equally.

ABSTRACT While chemical vapor deposition of diamond films is currently cost prohibitive for biosensor construction, in this paper, we show that sonication-assisted nanostructuring of biosensing electrodes with nanodiamonds (NDs) allows harnessing the hydrolytic stability of the diamond biofunctionalization chemistry for real-time continuous sensing, while improving the detector sensitivity and stability. We find that the higher surface coverages were important for improved bacterial capture and can be achieved through proper choice of solvent, ND concentration, and seeding time. A mixture of methanol and dimethyl sulfoxide provides the highest surface coverage ($33.6 \pm 3.4\%$) for the NDs with positive zeta-potential, compared to dilutions of dimethyl sulfoxide with acetone, ethanol, isopropyl alcohol, or water. Through impedance spectroscopy of ND-seeded interdigitated electrodes (IDEs), we found that the ND seeds serve as electrically conductive islands only a few nanometers apart. Also we show that the seeded NDs are amply hydrogenated to be decorated with antibodies using the UV-alkene chemistry, and higher bacterial captures can be obtained compared to our previously reported work with diamond films. When sensing bacteria from 10^6 cfu/mL *E. coli* O157:H7, the resistance to charge transfer at the IDEs decreased by $\sim 38.8\%$, which is nearly 1.5 times better than that reported previously using redox probes. Further in the case of 10^8 cfu/mL *E. coli* O157:H7, the charge transfer resistance changed by $\sim 46\%$, which is similar to the magnitude of improvement reported using magnetic nanoparticle-based sample enrichment prior to impedance detection. Thus ND seeding allows impedance biosensing in low conductivity solutions with competitive sensitivity.



KEYWORDS: nanodiamond · biosensing · bioimmobilization · impedance · surface chemistry

Microfabricated biosensor research and application has seen a rapid growth in the past decade, exploring a variety of nanomaterials to interface between biomolecules and electronics, although no clear evidence shows an advantage of a specific material.¹ Some of these new nanomaterials include carbon nanotubes,^{2–4} gold nanoparticles,^{5–7} zinc oxide nanorods,⁸ and graphene.^{9,10} In this paper, we report the first application of detonation nanodiamonds (NDs) to biosensing electrodes through a seeding process. We demonstrate that ND-seeded electrodes can be biofunctionalized using previously published UV-alkene surface chemistry of diamond films and used for pathogen detection.

Silicon surfaces and metal oxide nanomaterials have been attractive to create biosensors due to the existing semiconductor infrastructure.¹¹ However, the widely reported silane chemistry basis for anchoring biosensing molecules on silicon and metal

oxide nanomaterial biosensors is susceptible to hydrolysis in biological buffers and hence unstable.^{12,13} In contrast, chemical vapor deposition (CVD) diamond films composed predominantly of sp^3 -hybridized carbon atoms are known to have high chemical inertness and wide range of electrical conductivity.^{14–16} As an electrochemical electrode, CVD diamond has proven to be highly reproducible and stable over several months of storage in ambient air and produces low background (noise) and hence better detection limits than the conventional glassy carbon electrodes.^{17–19} Fujishima and co-workers have shown that diamond electrodes improve enzymatic biosensing of hydrogen peroxide and bisphenol A.^{20,21} Hamers and co-workers demonstrated label-free biosensing of protein–protein binding and DNA hybridization using diamond-based impedance biosensors and field-effect transistors.^{22,23} Hartl *et al.* showed that electrons can directly transfer between the redox center of the

* Address correspondence to radadia@latech.edu.

Received for review October 8, 2013 and accepted January 7, 2014.

Published online January 07, 2014
10.1021/nn405240g

© 2014 American Chemical Society

enzyme catalase and the nitrogen-doped diamond films (n-type, 1–3.33 $\Omega \cdot \text{cm}$) with a lower background current and a better stability than gold electrodes.²⁴ Recently, Nebel *et al.* showed that nanostructuring of the diamond electrodes with nanowires extends the electrochemical detection of complementary DNA down to 10 pM, which is 100 times smaller concentration compared to those demonstrated by gold electrodes.²⁵ Moreover, CVD diamond films have also been widely reported as biocompatible coatings during multiple *in vivo* studies on orthopedic^{26,27} and dental implants^{28,29} and *in vitro* studies.^{30–32} These findings also imply potential of diamond for cell-based biosensors or *in vivo* smart implants with sensors.

Additionally, among the many biomolecule immobilization chemistries of CVD diamond surfaces,^{16,33} the UV-alkene chemistry has gained considerable interest and has been reported to withstand severe hydrolysis conditions and result in better biomolecular stability.³⁴ During this chemistry, a 254 nm or smaller wavelength UV photon ejects electrons off the diamond surface carbon atoms into the adjacent alkene molecules, leading to covalent attachment of alkenes to the diamond carbon atom by the $\text{S}_{\text{N}}1$ reaction mechanism.^{35,36} Using this chemistry, Yang *et al.* have shown improved stability of DNA-modified diamond films to thermal cycling conditions over DNA-modified silicon, gold, glass, and glassy carbon surfaces.¹³ This is because the UV-alkene chemistry results in a hydrolytically stable C–C linkage that is able to withstand 30 times thermal cycling of hybridization–dehybridization of surface-bound DNA, while glass, gold, and silicon surfaces only lasted for five to 10 such cycles.³⁷ Recently, Radadia *et al.* immobilized antibodies to diamond films using the UV-alkene chemistry and tested its suitability for bacterial biosensing.^{34,38} Diamond surface chemistry showed improved temporal stability of antibodies compared to glass surfaces when exposed to saline media at 37 °C for prolonged periods extending up to 2 weeks. These studies show the potential of using diamond as an interfacing material for biosensor construction.

However, the use of diamond surface for biosensor construction is currently limited by (1) high-temperature requirement for growth (~ 700 °C), hence not allowing deposition on substrates with low melting point such as microscope slides, aluminum, or gold; and (2) high costs associated with the CVD process. CVD diamond films are synthesized by seeding a submonolayer of high-purity monocrystalline NDs as nucleation points, followed by its growth into a continuous film in methane, hydrogen, and argon gas flows using a hot filament CVD reactor or a microwave plasma CVD reactor. Thus, in this paper, we investigate the process of ND seeding as a means for creating lower-cost biosensors while leveraging benefits of the UV-alkene chemistry of diamond surfaces.

ND synthesis was discovered as a green chemistry in the late USSR in the 1960s while the shock compression of non-diamond carbon modifications in blast chambers was studied. The purification of the resulting mixture leads to colloidal suspensions of single-digit diamond particles with diameters of 4–5 nm.³⁹ Development of an environmentally friendly purification process has now allowed high-purity ND powders to be produced in large volumes at a low cost with controlled surface chemistry.⁴⁰ Seeding NDs with high density has been an area of much interest in CVD diamond film synthesis, and it has been explored extensively using sonication and electrophoretic deposition.^{41–44} During the sonication process, the collapse of microscopic cavitation bubbles causes acceleration of nanoparticles toward the substrates and lodges them on the substrate with a huge amount of pressure. Shenderova and co-workers provided details of solvent selection and ND concentrations on the coating process and resulting surfaces for CVD diamond growth.⁴⁵ Commercially, a large ultrasonic horn is used to uniformly seed NDs over the wafer; however, such high-power sonication is known to cause milling-induced mechanical damage to the substrate. To contrast, electrophoretic deposition can achieve higher surface coverage but requires a conductive substrate, hence it is unable to coat insulating substrates such as oxides. Schmidlin and co-workers recently demonstrated deposition of a 5 nm thick dense layer of NDs on highly oriented pyrolytic graphite through electrophoretic deposition from an ultracentrifuged suspension.⁴⁶ New techniques such as layer-by-layer assembly,^{47,48} inkjet printing,⁴⁹ and microcontact printing⁵⁰ have been reported to increase the seeding density. However, none of these methods have been evaluated by itself as a means to create biosensors. We chose a sonication-assisted seeding process as it allows even coating to nonconformal MEMS surfaces, while the sonication-related abrasion was reduced using a bath setup as described in the Methods section.

In this paper, we use the simplest yet versatile approach of low-power sonication-assisted seeding and report the effect of seeding solvents, concentrations, and time on ND surface coverage and capture capability as a pathogen sensor. Also, we apply the ND seeding technique to an interdigitated electrode (IDE) array, characterize the changes introduced by ND seeding at the IDEs using impedance spectroscopy, and finally demonstrate label-free pathogen detection upon biofunctionalization of ND-seeded IDEs.

RESULTS AND DISCUSSION

Monocrystalline NDs of an average particle size of 5 nm and a positive zeta-potential were obtained as 0.5 (w/v)% in dimethyl sulfoxide (DMSO). The highly polar S=O bond in DMSO is proposed to form strong hydrogen bonds with acidic hydrogen atoms of the

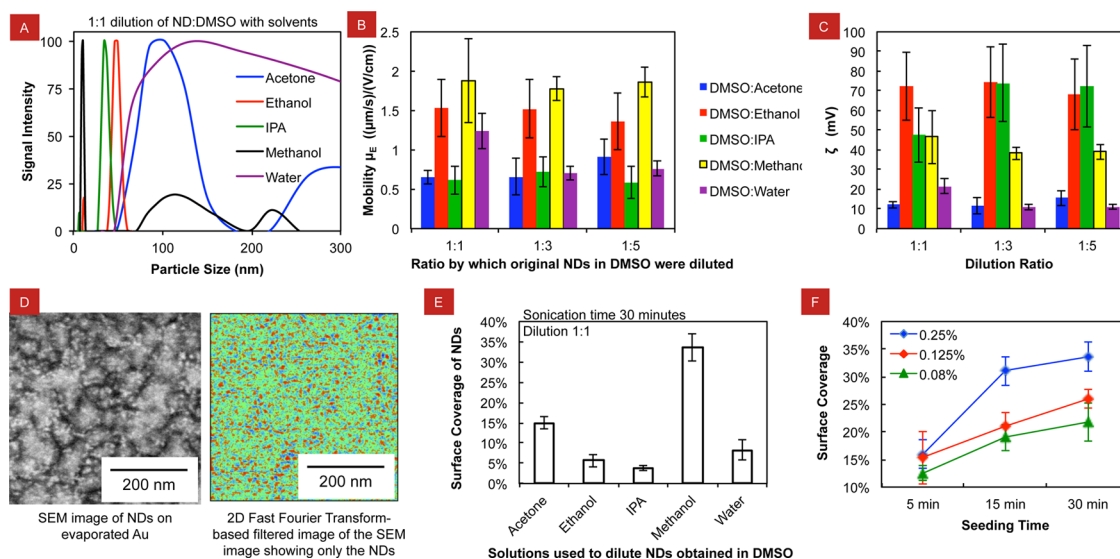


Figure 1. Measurement of (A) ND particle sizes, (B) mobility (μ_e), and (C) zeta-potential (ζ) after dilution of the original ND-containing DMSO with acetone, ethanol, isopropyl alcohol (IPA), methanol, and water. Average values are reported from five repeats. (D) On the left is the SEM image showing NDs (bright white spots) seeded on gold surfaces by sonication in solution containing NDs at 0.25% (w/v) for 30 min. On the right is the SEM image after 2D FFT filtering highlights the seeded NDs as red regions. (E) Surface coverage obtained on gold surfaces by sonication in ND solution diluted with acetone, ethanol, IPA, methanol, and water. (F) Surface coverage of NDs obtained on surfaces seeded for varying amounts of times with methanol solutions containing 0.25, 0.125, and 0.08% (w/v) NDs.

hydroxyl groups or the protonated forms of pyrone-like structures that are hypothesized to exist on the surface of NDs with positive zeta-potential; thus a more stabilized ND suspension is formed in DMSO.⁴⁵ Seeding of ND is typically carried out in alcohols, ketones, DMSO, water, or their mixtures to reduce surface tension, viscosity, volatility, boiling point, or environmental hazards specifically in the case of water. Shenderova and co-workers have reported dilution of DMSO with methanol to produce the best seeding.⁴⁵ As shown in Figure 1A, we found photon correlation spectroscopy shows that the 1:1 dilution of ND/DMSO with acetone, ethanol, IPA, methanol, or water leads to formation of ND aggregates when sonicated for 30 min and rest for 1 h before particle size measurements in each case. Similar results were also achieved with 1:3 and 1:5 dilutions as shown in Supporting Information Figure S1. Solvent properties used for calculating aggregate sizes *via* photon correlation spectroscopy were estimated using molar ratios and are listed in Table S1.

It is believed that in the case of polar protic solvent addition to DMSO, the aggregation of NDs occurs through displacement of polar aprotic DMSO molecules in the solvation sphere that is around the ND, by polar protic molecules of ethanol, IPA, methanol, or water, and then this catalyzes the ND aggregation through hydrogen bonding.⁴⁵ The extent of ND aggregate size is also dependent on factors such as viscosity, density, and surface tension. We further measured electrophoretic mobility in each case (Figure 1B) and calculated zeta-potentials (ζ) of the ND aggregates (Figure 1C). We find that the electrophoretic mobility is highest in the case of methanol followed by ethanol.

Zeta-potential calculations show that the suspensions of ND aggregates are stable ($\zeta > 20$ mV) in the case of dilution with alcohols compared to dilutions with acetone or water. This shows that, although NDs clump together on addition of alcohols, the suspension will provide a stronger resistance to sedimentation in alcohols compared to water and acetone. These results also have implications on conditions to use for electrophoretic deposition of NDs with positive zeta-potentials.

Further, we seeded the NDs on 200 nm thin evaporated gold films on silicon substrates *via* sonication in ND/DMSO diluted with acetone, ethanol, IPA, methanol, and water. See Methods section for specific procedure on seeding and analysis of coverage on seeded substrates. Figure 1D (left image) shows a representative SEM image obtained for surfaces seeded for 30 min with a ND/DMSO diluted (1:1) with methanol. NDs show up as bright white spots in the SEM image. The large white grains in the background are the evaporated gold clusters. It can be seen that NDs were seeded continuously and uniformly irrespective of the topography of underlying gold film; no clustering of NDs was found at the grain boundaries of gold in the case of methanol. In order to further extract information on seeding coverage and average seed size, a two-dimensional fast Fourier transform-based filtering was performed to remove the gold background. Figure 1D (right image) shows the SEM image obtained upon filtering. Figure 1E shows the surface coverage obtained with 30 min seeding with a 1:1 dilution of ND/DMSO with acetone, ethanol, IPA, methanol, and water. We find that methanol provides the highest surface

coverage ($33.6 \pm 3.4\%$) compared to the other solvents. We believe methanol dilutions lower the surface tension, solution viscosity, and solution density and provide the correct surface forces, while maintaining the small size of the NDs and the high surface area to volume ratio; thus methanol dilutions create the correct proportion of dispersion, polar, and hydrogen bonding forces to lodge particles onto the surface with highest surface coverage.

Thus we have shown that, with our low-power sonication setup, methanol produces better surface coverage among the many solvents used for ND seeding. Hence we used methanol dilutions of ND/DMSO for further work in this paper. In an attempt to reduce the seeding times, Figure 1E shows a plot of ND surface coverage on surfaces seeded with solutions of three different ND concentrations (0.25, 0.125, 0.083% w/v) for three different seeding times (5, 15, and 30 min). As expected, we find that the surface coverage increased with ND concentration and seeding time. We expected the surface coverage to plateau at some point of time, and this time point would be earlier for high concentration solutions. We found that, while using the 0.25% (w/v) solution, the seeding coverage starts to plateau to about 33% coverage at 30 min seeding, while plateau points were not obtained for 0.125 and 0.083% (w/v) solutions within 30 min of seeding. We believe that seeding times can be further reduced through the use of ND concentrations higher than 0.25% (w/v).

Figure 2 confirms that ND-seeded surfaces can be functionalized using previously reported UV-alkene surface chemistry of CVD diamond films. Surface modification was tested by attachment of FITC-conjugated anti-*E. coli* (O+K) and measuring the fluorescence intensity, as shown in Figure 2A. Antibodies were spotted in a 10×10 array using a Nano eNabler ($\sim 12 \mu\text{m}$ spot size). Since the functionalization scheme relies on the presence of hydrogenated carbon atoms, we also explored the effect of sodium borohydride assisted mild reduction for improvements expected through an increase in antibody attachment. See Figure 2B. Quantification of the fluorescence from spotted arrays, as shown in Figure 2C, shows that the reduction step does not provide the anticipated enhancement in fluorescence. This shows that the as-seeded NDs were adequately hydrogenated for the UV-alkene chemistry. In our experiments, control surfaces (without NDs) record any fluorescence with our microscopes, proving insignificant attachment of antibodies. Figure 3 shows the effect of surface coverage of NDs on the bacteria capture capability from solutions of different bacterial concentrations (10^5 , 10^6 , and 10^7 cells/mL). Heat-inactivated *E. coli* O157:H7 were used along with a specific antibody for these experiments. The bacteria capture density was found to increase with surface coverage of NDs. We were

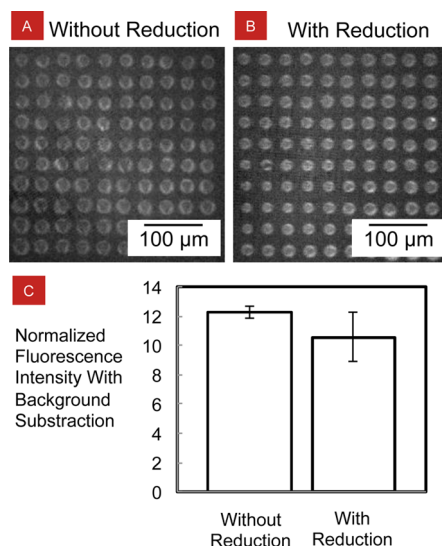


Figure 2. Fluorescence images obtained from a 10×10 array of $12 \mu\text{m}$ spots of FITC-labeled anti-*E. coli* O+K attached to ND-seeded surfaces without (A) and with (B) sodium borohydride reduction treatment prior to performing UV-assisted TFAAD linkage to NDs. (C) Normalized fluorescence intensity obtained from seven 10×10 arrays on the ND surface with and without reduction.

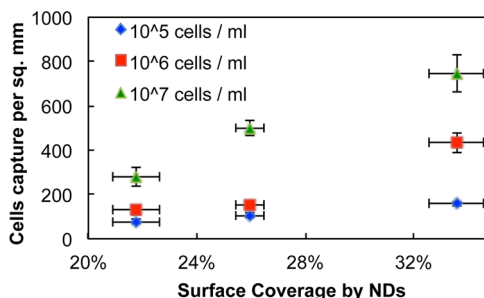


Figure 3. Bacteria capture density obtained using the antibody-ND coating as a function of surface coverage of NDs on the sample.

expecting that the bacteria capture density would plateau for higher surface coverage values; however, we must not have reached high enough ND surface coverage to achieve the plateau point. Nevertheless, the capture densities obtained were about 800 cells/ mm^2 , which is higher than that reported previously with diamond surfaces for the exact same antibody–antigen pair.³⁸

Figure 4A shows the microfabricated 3×3 IDE array seeded with NDs using the above recipe that gave us the highest surface coverage. The electrodes were fabricated of 200 nm Au/25 nm Cr, and each finger is $9 \mu\text{m}$ thick with $9 \mu\text{m}$ spacing. PECVD oxide was coated to insulate the wiring from the solution, and a circular window in the oxide was opened to expose the IDEs to the solution. In order to elucidate the effect on IDE nanostructuring via ND seeding, we performed impedance measurements in solutions with varying conductivity before and after ND seeding. Impedance spectra of IDEs in deionized water (as shown in Figure 4B)

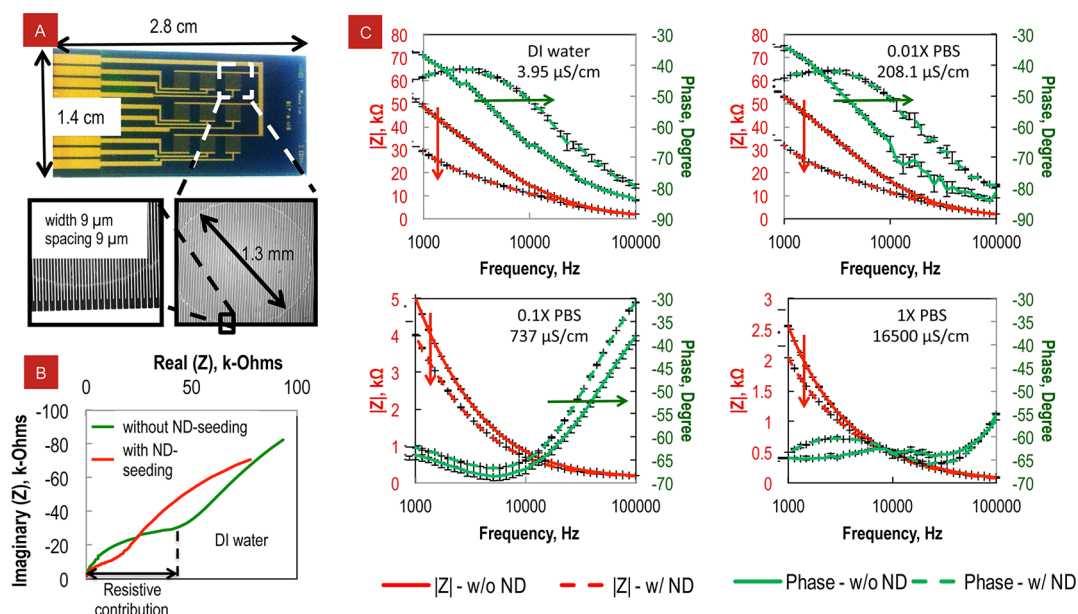


Figure 4. (A) Optical images of a biosensor chip containing an array of nine interdigitated electrode (IDE) pairs that were fabricated to demonstrate the application of ND seeding layer for chemically stable covalent linkage of antibodies to electrodes. Each IDE contained 60 finger pairs with each finger $9\ \mu\text{m}$ wide and spaced $9\ \mu\text{m}$ apart. (B) Representative plot of real versus imaginary part of the impedance measured in deionized water on an IDE before and after ND seeding. (C) Representative plot of impedance magnitude and phase plotted against frequency as obtained on an IDE exposed to solutions with different electrical conductivity.

shows that the resistive or the charge transfer contribution to the overall impedance decreased with ND seeding. This implies that the ND seeds form electrically conductive islands between the electrode fingers. This is consistent with previous reports that hydrogen-terminated diamond surfaces become conductive when exposed to water.⁵¹ Figure 4C shows that the decrease in overall impedance and shift in phase at the IDEs upon ND seeding were consistently seen in deionized water and phosphate buffered saline (PBS) dilutions. Moreover, as the solution became more conductive, the charge transfer took place less through surface conduction and more through solution conductance. Specifically, at 1000 Hz, the reduction in magnitude of impedance due to ND seeding changes from 40 to 20% as the solution conductivity increases from 3.95 to 16500 $\mu\text{S}/\text{cm}$. Typically, in impedance spectroscopy, the conductivity of the solution is adjusted through addition of potassium chloride to achieve an overall magnitude in the range of 10 to 30 k Ω prior to carrying out detection. We show that ND seeding can be used to lower the required impedance without altering the solution conductivity, thus increasing the potential to combine impedance spectroscopy with on-chip preconcentration mechanisms like dielectrophoresis that require low conductivity solutions.

Further, we seeded IDEs with NDs to create nonfaradaic impedance biosensors for bacterial detection without using redox probes, where the capture agent was immobilized on the NDs with the UV-alkene surface chemistry. The IDE portion of the chip was seeded

with NDs, followed by selective functionalization of some of the IDEs with anti-*E. coli* O157:H7 as described in the Methods section. Further, we also created two control IDEs by skipping the antibody attachment step. A polydimethylsiloxane well was then applied on the IDE region, and bacteria were captured from solution containing 10^6 or 10^8 cells/mL. Changes in overall impedance and phase across each of the IDEs were recorded over a frequency range from 100 to 10^5 Hz. Figure 5A shows sample magnitude and phase curves obtained on one of the active sensors. Although we observed insignificant shifts in impedance magnitude, we saw significant phase shifts on all of the active sensors; such phase shifts were not seen on control sensors. In order to understand the physical basis of the impedance changes, the response of the interface was compared with a variety of different equivalent circuit models including those discussed by Varshney and Li.⁵² While a number of models were investigated by complex nonlinear least-squares fitting using Zview, the circuit shown in Figure 5B provided a good fit to the data with a reasonable number of components with errors less than 5%. The equivalent circuit model consists of a double-layer capacitance, C_{dl} , a generalized finite Warburg element for a short circuit terminus, W_s ($Z = R \tanh([\sqrt{i\omega}]^p)/[\sqrt{i\omega}]^p$) with a continuously varying exponent ($0 < p < 1$), a charge transfer resistance, R_{ct} , a solution resistance, R_s , and a resistance, R_f , and capacitance, C_f , arising due to the presence of the functionalization layer including the antibody and the blocker protein molecules. During the dissociation of

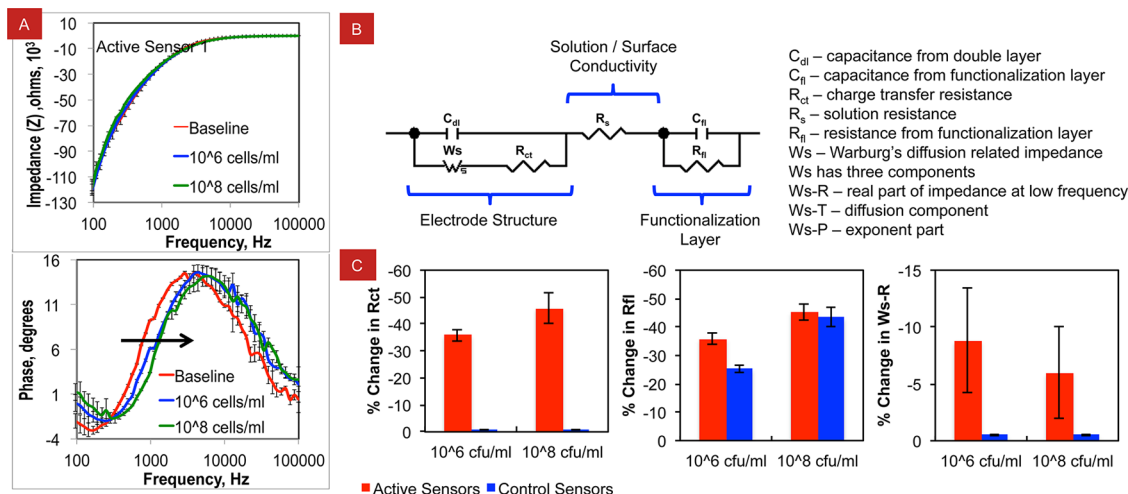


Figure 5. (A) Example impedance spectra on active sensors before (baseline) and after exposure to 10^6 or 10^8 cells/mL of *E. coli* O157:H7 cells. (B) Modified Randles circuit that best fits our impedance results. (C) Significant changes observed in charge transfer resistance (R_{ct} , R_{fi} , and W_s -R) upon binding of bacterial cells to the sensor surface.

TABLE 1. Equivalent Circuit Fit Values for One of the Active and Control Sensors

parameters	active sensor			control sensor		
	after antibody immobilization and blocking with casein	after capture from 10^6 cfu/mL	After capture from 10^8 cfu/mL	after antibody immobilization and blocking with casein	after capture from 10^6 cfu/mL	after capture from 10^8 cfu/mL
R1 (Ω)	12541	7864	6864	~0	~0	~0
R2 (Ω)	1807	1176	932.3	1713	1259	913
Ws1-R (Ω)	536160	497200	512230	999220	980110	982310
Ws1-T		4.9×10^{-3}			7.2×10^{-3}	
Ws1-P		0.77			0.56	
R2 (Ω)		25			25	
C1 (F)		2.4×10^{-9}			2.2×10^{-9}	
C2 (F)		1.38×10^{-9}			1.4×10^{-9}	

pure water through $2\text{H}_2\text{O} \rightarrow \text{H}_3\text{O}^+ + \text{OH}^-$, a total ion concentration (c) of 2×10^{-7} mol/L can be achieved, and hence the maximum Debye length achieved is ($\lambda = 0.3/\sqrt{c} = 680$ nm at 20°C). However, in deionized water that we used, due to the presence of impurities, we can expect Debye lengths of a few hundred nanometers. Because the Debye screening length is comparable to the height at which antibody binds to the cell surface, the resistance and capacitance of the functionalization layer have been considered discretely, as shown in Figure 5B.

Equivalent circuit fits obtained for one of the active and the control sensors are given in Table 1. Fit results for other active and control sensors are provided in Tables S2 and S3 in the Supporting Information, respectively. We found that the parameters R_{ct} , R_{fi} , and W_s -R change by more than 5% during the cell capture process with respect to the values obtained after antibody functionalization and blocking, as shown in Figure 5C. The values for R_{ct} decreases by 38.8 ± 2.3 and $45.9 \pm 5.8\%$ only on the active sensors during the capture from 10^6 and 10^8 cfu/mL, respectively, with a minimal change of 6.5% between the two concentrations.

We believe that this reduction in R_{ct} is because the bacterial attachment causes nonflagellar protein filaments (pili and fimbriae) and lipopolysaccharides, all primarily negatively charges in the case of *E. coli* O157:H7, to replace the less electrically conductive water molecules and lower the charge transfer resistance. This process also reduces the effective diffusion length between adjacent electrodes, and thus we also see a decrease in the Warburg diffusion element W_s -R. The values for the exponent P were found to be higher than 0.5, which suggests the existence of charge transfer mechanisms other than pure diffusion between the two ND-seeded electrodes. We also found that value of R_{fi} also reduces during the cell capture steps; however, this drop was also seen on the control sensors. We believe the reduction in R_{fi} is due to the loss of casein blocker molecules during the repetitive washing steps post-cell-capture to remove nonspecifically bound bacteria.

We find that the change in R_{ct} obtained using the ND-seeded gold electrodes for 10^6 cfu/mL *E. coli* O157:H7 ($\sim 38.8\%$) is nearly 1.5 times higher than the 27.8% change reported by Yang *et al.* using indium tin oxide (ITO) impedance biosensor in combination

with $[\text{Fe}(\text{CN})_6]^{3-/4-}$ redox probes.⁵³ In the case of ND-seeded electrodes, the sensor was exposed to 200 μL in a PDMS well, while Yang *et al.* evaporated the 20 μL pure culture on the sensor. We also find that the changes in R_{ct} obtained using a ND-seeded biosensor for 10^8 cfu/mL *E. coli* O157:H7 (~46%) is nearly 225% of those reported by Varshney and Li using gold impedance biosensors (–20.9%).⁵⁴ Varshney and Li only saw such magnitude of improvement when magnetic nanoparticle-based sample enrichment was performed prior to impedance detection. Moreover, one of the active sensors in our test was later tested after storage in ITS at room temperature for a four day test, and the fit results were found to be comparable to those of the fresh sensors. We are currently working to perform extensive testing on the stability of antibodies on ND-seeded gold surfaces. Similarly, while our tests here were limited primarily to 10^6 and 10^8 cfu/mL, and detection limits were not evaluated, we are currently working on combining the ND-seeded biosensors with the use of redox probes, microfluidics, and preconcentration techniques such as dielectrophoresis or magnetophoresis for real-time pathogen sensing.

CONCLUSIONS

In summary, we have demonstrated a new method using nanodiamond seeding to immobilize antibodies

on impedance biosensors and improve the overall detection sensitivity than that obtained with gold or ITO electrodes. We show that methanol forms the ideal solvent in seeding gold sensing surfaces with NDs with positive zeta-potential, in comparison to solvents such as acetone, ethanol, IPA, and deionized water. Further, the seeding has to be performed in solutions with higher ND concentration and for seeding times as long as 30 min to produce maximum surface coverage and to consecutively achieve maximum bacterial capture density. We also show that these NDs with positive zeta-potential can be functionalized with the UV-alkene chemistry without a further reduction step. NDs when seeded at IDEs act as electrically conductive islands between the electrodes and reduce the effective gap between the electrodes, thus allowing performance of impedance spectroscopy in solutions with low electrical conductivity such as ITS. This ND seeding procedure along with the UV-alkene chemistry is applicable to a wide range of sensing methodologies including quartz crystal microbalance, surface plasmon resonance, microarray technology, and electrochemical sensing. We find that bacterial sensing can be performed in ITS and the changes obtained in resistance to charge transfer with bacterial capture is nearly twice that obtained with plain electrodes.

METHODS

Materials. All stock solutions were prepared by deionized water from a Millipore deionization system to obtain minimum resistivity of 18.0 $\text{M}\Omega \cdot \text{cm}$. Sodium borohydride, 1-dodecene, glutaraldehyde (50%), sodium cyanoborohydride coupling buffer, casein blocking solution, and 3,3'-dihexyloxycarbocyanine iodide stain (DiOC6(3)) were bought from Sigma Aldrich. Phosphate buffered saline (PBS), PBS with Tween 20 (PBS-T20), and bovine serum albumin (BSA) were bought from Bioexpress. Methanol, chloroform, isopropyl alcohol (IPA), and polydimethylsiloxane (PDMS) were obtained from Fisher Scientific. NDs were purchased from International Technology Center in the form of 0.5 w/v% nanocrystalline diamond (Blue seeds) solution. *E. coli* O157:H7 antibodies were bought from Kirkegaard & Perry Laboratories, and anti-*E. coli* O+K FITC conjugate was bought from Pierce Thermo Scientific.

ND Seeding and Analysis. Silicon wafer with evaporated gold (200 nm Au/25 nm Cr) was diced into 1 cm \times 1 cm pieces that were used as substrates for ND seeding. The as-obtained ND solution consisted of 0.5 w/v% of average 5 nm monocrystalline diamonds in dimethylsulfoxide (DMSO). According to the manufacturer, the NDs were size separated by centrifugation and were found to be within 3–10 nm while the peak of the distribution was around 5 nm. These NDs show a positive zeta-potential, and DMSO as a solvent provides strong resistance to settling of these NDs.⁴⁵ As-obtained ND solution was diluted with acetone, ethanol, IPA, methanol, or water in 1:1, 1:3, or 1:5 ratio. Brookhaven Instruments ZetaPlus was used to measure the zeta-potential and make particle size measurements using dynamic light scattering ($\lambda = 660$ nm). The zeta-potential calculations were performed using the Smoluchowski equation because the ND particles were of wide size range (10–200 nm). Use of Huckel approximation did not change the trend seen in the zeta-potential measurements. For sonication treatment,

samples were immersed in ND-containing solutions in a tightly sealed 20 mL scintillation vial, and the vials were placed in a Branson 5510 sonication bath (40 kHz, 185 W) equipped with a stainless steel basket. We have used a very low power sonication approach as opposed to the relatively high sonication power immersion horns used commercially. This way we reduced abrasion of gold electrodes. After sonication for the required amount of time, the seeded substrates were cleaned with methanol, deionized water, and isopropyl alcohol and blow-dried with nitrogen. Surface morphology of nanocrystalline diamond-seeded surface was investigated using Hitachi S-4800 field emission scanning electron microscopy (SEM) and further 2D fast Fourier transform filtering of the SEM images using the Gwyddion software package.

Functionalization of NDs. Some of the ND-seeded surfaces were reduced in 65 mM sodium borohydride solution in methanol at 70 $^{\circ}\text{C}$ for 6 h. Trifluoroacetamide-protected 10-aminodec-1-ene (TFAAD) was mixed with 1-dodecene in 2:1 ratio (v/v) to form the functionalization mix. The 1-dodecene spaces the TFAAD molecules and enhances the efficiency of deprotection in the subsequent step to UV functionalization. The photochemistry attachment was carried out in a nitrogen-purged reaction chamber. Functionalization mix at about 2 $\mu\text{L}/\text{cm}^2$ was applied uniformly between the ND-seeded surface and a piranha-cleaned quartz slide, then radiated with 254 nm UV at ~ 2 mW/cm^2 for 6 h. Excess reaction mix was removed by sonication in chloroform and IPA for 5 min each. The trifluoroacetic acid group from the functionalized surfaces was deprotected in a tight-sealed vial containing 65 mM sodium borohydride in anhydrous methanol for 6 h at 70 $^{\circ}\text{C}$.⁵⁵ The sample was then rinsed with deionized water and dried with nitrogen, and the primary amine groups on the sample surface were then reacted with glutaraldehyde in a sodium cyanoborohydride coupling buffer at room temperature for 4 h to yield an aldehyde termination by reductive amination.⁵⁶

The aldehyde-terminated surface was rinsed with deionized water and dried with nitrogen. The functionalized surface was incubated for 18–22 h at 4 °C with a 100 $\mu\text{g/mL}$ antibody solution, which was printed using a Nano eNabler. The Nano eNabler uses microcantilevers containing a microfluidic channel that delivers solutions from the reservoir to the tip. We used tips that had 30 μm wide channels. After printing, a PDMS well was placed over the printed region and a coverslip to prevent evaporation. Next day, the wells were washed with PBS-T20 twice and PBS once to remove nonspecifically adsorbed antibodies. Further nonspecific binding sites were blocked with a casein blocking buffer for 1 h at room temperature. The well was then washed again with PBS-T20 twice and PBS once to remove excess casein. The normalized fluorescence intensity shown in Figure 2 with background subtraction was obtained from seven 10×10 arrays on nanocrystalline diamond-seeded surface with or without reduction treatment.

Fluorescent Labeling of Bacteria. *E. coli* O157:H7 was inoculated in Luria–Bertani broth (LB) at 37 °C for 12 h. Based on plating culture at the 12th hour, all bacteria were found to reach a stationary phase of growth. The concentration of the labeled culture was estimated by agar plating of the 10^{-5} and 10^{-6} dilution. Culture at the 12th hour was washed with phosphate buffered saline (PBS) through pelleting (12k rpm, 2 min) and suspension in fresh PBS. Heat-inactivated bacteria (70 °C for 15 min) were used for work in this paper. Labeling was performed by mixing 2 μL of DiOC6(3) (5 mg/mL) in the inactivated culture at 37 °C incubator for 30 min. Excess labeling dye was removed by pelleting and suspension in fresh PBS. The labeled culture was then suspended in PBS prior to capture studies.

Bacteria Capture Experiment. A 100 μL solution of 10^5 , 10^6 , and 10^7 cells/mL was deposited in the PDMS wells, which were attached on the antibody-functionalized ND surface. A coverslip was placed on the top of the PDMS well to prevent evaporation. The surface exposed to the bacterial solution was placed in the 37 °C incubator for 30 min. Then the surfaces were washed with PBS (three times) to remove non-specific-bound bacteria. For use with an electrical biosensor, isotonic trehalose solution was used instead of PBS to reduce the conductivity of the media. The surface-captured bacteria were imaged using an Olympus BX41 fluorescence microscope equipped with a Photometrics Cool-snap K4 camera and enumerated using ImageJ. We collected five images for each of the nine NCD samples. With the biosensor, we could not image the fluorescent bacteria due to high reflectivity of the gold electrodes.

Biosensor Fabrication and Testing. Biosensor substrates consisted of 525 μm thick silicon with a 280 nm thick thermal oxide layer. The gold/chrome (200 nm/25 nm) was patterned through lift-off processing. A 300 nm thin PECVD oxide layer was deposited on the gold pattern as an insulation layer. Circular windows were opened in the insulation layer by buffered oxide etching to expose the interdigitated electrodes. Electrical connections were made using a high-density card-edge connector. Impedance measurements were made with a CompactStat (Ivium Technologies). The excitation voltage was limited to 10 mV to prevent the restructuring or delamination of the gold electrodes, the denaturing of attached biomolecules, or electroporation of capture bacteria. Control measurements were made using isotonic trehalose solution (ITS) that measured a conductivity of 3 $\mu\text{S/cm}$. First impedance measurements were made after exposing the sensor to 10^6 cells/mL ITS for 1 h, followed by rinsing with ITS three times. Subsequently, the sensor was exposed to 10^8 cells/mL ITS for 1 h, followed by rinsing with ITS three times and impedance measurement again. We could not get a count of bacteria capture density at the IDEs due to the high reflection of gold saturating most of the region during fluorescence imaging.

Conflict of Interest: The authors declare no competing financial interest.

Acknowledgment. This material is based upon work partly supported by the National Science Foundation under Grant Number 1062937. Any opinions, finding, and conclusions or recommendations expressed in this material are those of the authors and do not necessarily reflect the views of the National

Science Foundation. Authors are grateful to R. Bashir (Illinois) and A. Bhunia (Purdue) for sharing *E. coli* cultures, and to R. Hamers (Wisconsin—Madison) for sharing the UV-alkene chemistry process and chemicals. Research reported in this publication was also partly supported by an Institutional Development Award (IDeA) from the National Institute of General Medical Sciences of the National Institutes of Health under Grant Number P20GM103424.

Supporting Information Available: Results from photon correlation spectroscopy, properties of solvent mixtures used to calculated ND aggregate size and zeta-potentials, and equivalent circuit fit values obtained for other active and control sensors. This material is available free of charge via the Internet at <http://pubs.acs.org>.

REFERENCES AND NOTES

- Andrescu, D.; Andrescu, S.; Sadik, O. A. New Materials for Biosensors, Biochips and Molecular Bioelectronics. In *Biosensors and Modern Biospecific Analytical Techniques*; Gorton, L., Ed.; Elsevier: Amsterdam, 2005; Vol. 285.
- Basuray, S.; Senapati, S.; Aijian, A.; Mahon, A. R.; Chang, H.-C. Shear and AC Field Enhanced Carbon Nanotube Impedance Assay for Rapid, Sensitive, and Mismatch-Discriminating DNA Hybridization. *ACS Nano* **2009**, *3*, 1823–1830.
- Chen, Y.; Lee, Y. D.; Vedala, H.; Allen, B. L.; Star, A. Exploring the Chemical Sensitivity of a Carbon Nanotube/Green Tea Composite. *ACS Nano* **2010**, *4*, 6854–6862.
- Song, H. S.; Kwon, O. S.; Lee, S. H.; Park, S. J.; Kim, U.-K.; Jang, J.; Park, T. H. Human Taste Receptor-Functionalized Field Effect Transistor as a Human-like Nanobioelectronic Tongue. *Nano Lett.* **2013**, *13*, 172–178.
- Wang, M.; Wang, L.; Wang, G.; Ji, X.; Bai, Y.; Li, T.; Gong, S.; Li, J. Application of Impedance Spectroscopy for Monitoring Colloid Au-Enhanced Antibody Immobilization and Antibody–Antigen Reactions. *Biosens. Bioelectron.* **2004**, *19*, 575–582.
- Li, C.-Z.; Liu, Y.; Luong, J. H. Impedance Sensing of DNA Binding Drugs Using Gold Substrates Modified with Gold Nanoparticles. *Anal. Chem.* **2005**, *77*, 478–485.
- Szymanska, I.; Radecka, H.; Radecki, J.; Kalisz, R. Electrochemical Impedance Spectroscopy for Study of Amyloid B-Peptide Interactions with (–)Nicotine Ditartrate and (–)Cotinine. *Biosens. Bioelectron.* **2007**, *22*, 1955–1960.
- Choi, S.-H.; Ankonina, G.; Youn, D.-Y.; Oh, S.-G.; Hong, J.-M.; Rothschild, A.; Kim, I.-D. Hollow ZnO Nanofibers Fabricated Using Electrospun Polymer Templates and Their Electronic Transport Properties. *ACS Nano* **2009**, *3*, 2623–2631.
- Fowler, J. D.; Allen, M. J.; Tung, V. C.; Yang, Y.; Kaner, R. B.; Weiller, B. H. Practical Chemical Sensors from Chemically Derived Graphene. *ACS Nano* **2009**, *3*, 301–306.
- Robinson, J. T.; Perkins, F. K.; Snow, E. S.; Wei, Z.; Sheehan, P. E. Reduced Graphene Oxide Molecular Sensors. *Nano Lett.* **2008**, *8*, 3137–3140.
- Weetall, H. H. Preparation of Immobilized Proteins Covalently Coupled through Silane Coupling Agents to Inorganic Supports. *Appl. Biochem. Biotechnol.* **1993**, *41*, 157–188.
- Seitz, O.; Fernandes, P. G.; Tian, R.; Karnik, N.; Wen, H.-C.; Stiegler, H.; Chapman, R. A.; Vogel, E. M.; Chabal, Y. J. Control and Stability of Self-Assembled Monolayers under Biosensing Conditions. *J. Mater. Chem.* **2011**, *21*, 4384–4392.
- Yang, W.; Auciello, O.; Butler, J. E.; Cai, W.; Carlisle, J. A.; Gerbi, J. E.; Gruen, D. M.; Knickerbocker, T.; Lasseter, T. L.; Russell, J. N. DNA-Modified Nanocrystalline Diamond Thin-Films as Stable, Biologically Active Substrates. *Nat. Mater.* **2002**, *1*, 253–257.
- Granger, M. C.; Witek, M.; Xu, J.; Wang, J.; Hupert, M.; Hanks, A.; Koppang, M. D.; Butler, J. E.; Lucazeau, G.; Mermoux, M. Standard Electrochemical Behavior of High-Quality, Boron-Doped Polycrystalline Diamond Thin-Film Electrodes. *Anal. Chem.* **2000**, *72*, 3793–3804.

15. Swain, G. M.; Ramesham, R. The Electrochemical Activity of Boron-Doped Polycrystalline Diamond Thin Film Electrodes. *Anal. Chem.* **1993**, *65*, 345–351.
16. Nebel, C. E.; Shin, D.; Rezek, B.; Tokuda, N.; Uetsuka, H.; Watanabe, H. Diamond and Biology. *J. R. Soc., Interface* **2007**, *4*, 439–461.
17. Rao, T. N.; Yagi, I.; Miwa, T.; Tryk, D. A.; Fujishima, A. Electrochemical Oxidation of NADH at Highly Boron-Doped Diamond Electrodes. *Anal. Chem.* **1999**, *71*, 2506–2511.
18. Sarada, B. V.; Rao, T. N.; Tryk, D. A.; Fujishima, A. Electrochemical Oxidation of Histamine and Serotonin at Highly Boron-Doped Diamond Electrodes. *Anal. Chem.* **2000**, *72*, 1632–1638.
19. Foord, J. S. Diamond Electrochemical Sensors. In *CVD Diamond for Electronic Devices and Sensors*; John Wiley & Sons Ltd.: New York, 2009; pp 439–465.
20. Notsu, H.; Tatsuma, T.; Fujishima, A. Tyrosinase-Modified Boron-Doped Diamond Electrodes for the Determination of Phenol Derivatives. *J. Electroanal. Chem.* **2002**, *523*, 86–92.
21. Tatsuma, T.; Mori, H.; Fujishima, A. Electron Transfer from Diamond Electrodes to Heme Peptide and Peroxidase. *Anal. Chem.* **2000**, *72*, 2919–2924.
22. Yang, W.; Butler, J. E.; Russell, J. N.; Hamers, R. J. Interfacial Electrical Properties of DNA-Modified Diamond Thin Films: Intrinsic Response and Hybridization-Induced Field Effects. *Langmuir* **2004**, *20*, 6778–6787.
23. Yang, W.; Hamers, R. J. Fabrication and Characterization of a Biologically Sensitive Field-Effect Transistor Using a Nanocrystalline Diamond Thin Film. *Appl. Phys. Lett.* **2004**, *85*, 3626–3628.
24. Hartl, A.; Schmich, E.; Garrido, J. A.; Hernando, J.; Catharino, S. C.; Walter, S.; Feulner, P.; Kromka, A.; Steinmuller, D.; Stutzmann, M. Protein-Modified Nanocrystalline Diamond Thin Films for Biosensor Applications. *Nat. Mater.* **2004**, *3*, 736–742.
25. Yang, N.; Uetsuka, H.; Osawa, E.; Nebel, C. E. Vertically Aligned Diamond Nanowires for DNA Sensing. *Angew. Chem., Int. Ed.* **2008**, *47*, 5183–5185.
26. Narayan, J.; Fan, W. D.; Narayan, R. J.; Tiwari, P.; Stadelmaier, H. H. Diamond, Diamond-like and Titanium Nitride Biocompatible Coatings for Human Body Parts. *Mater. Sci. Eng., B* **1994**, *25*, 5–10.
27. Tang, L.; Tsai, C.; Gerberich, W. W.; Kruckeberg, L.; Kania, D. R. Biocompatibility of Chemical-Vapour-Deposited Diamond. *Biomaterials* **1995**, *16*, 483–488.
28. Rupperecht, S.; Bloch, A.; Rosiwal, S.; Neukam, F. W.; Wiltfang, J. Examination of the Bone–Metal Interface of Titanium Implants Coated by the Microwave Plasma Chemical Vapor Deposition Method. *Int. J. Oral Maxillofac. Implants* **2002**, *17*, 778–785.
29. Bacakova, L. Nanodiamond as Promising Material for Bone Tissue Engineering. *Nanosci. Nanotechnol.* **2009**, *9*, 3524–3534.
30. Bajaj, P.; Akin, D.; Gupta, A.; Sherman, D.; Shi, B.; Auciello, O.; Bashir, R. Ultrananocrystalline Diamond Film as an Optimal Cell Interface for Biomedical Applications. *Biomed. Microdevices* **2007**, *9*, 787–794.
31. Gorausova, L.; Kromka, A.; Burdikova, Z.; Eckhardt, A.; Rezek, B.; Vacik, J.; Haenen, K.; Lisa, V.; Bacakova, L. Enhanced Growth and Osteogenic Differentiation of Human Osteoblast-like Cells on Boron-Doped Nanocrystalline Diamond Thin Films. *PLoS One* **2011**, *6*, 1–17.
32. Shi, B.; Jin, Q.; Chen, L.; Auciello, O. Fundamentals of Ultrananocrystalline Diamond (UNCD) Thin Films as Biomaterials for Developmental Biology: Embryonic Fibroblasts Growth on the Surface of (UNCD) Films. *Diamond Relat. Mater.* **2009**, *18*, 596–600.
33. Garrido, J. A. Biofunctionalization of Diamond Surfaces: Fundamentals and Applications. In *CVD Diamond for Electronic Devices and Sensors*; John Wiley & Sons Ltd.: New York, 2009; pp 399–437.
34. Stavis, C.; Clare, T. L.; Butler, J. E.; Radadia, A. D.; Carr, R.; Zeng, H.; King, W. P.; Carlisle, J. A.; Aksimentiev, A.; Bashir, R. Surface Functionalization of Thin-Film Diamond for Highly Stable and Selective Biological Interfaces. *Proc. Natl. Acad. Sci. U.S.A.* **2011**, *108*, 983–988.
35. Colavita, P. E.; Sun, B.; Tse, K.-Y.; Hamers, R. J. Photochemical Grafting of *n*-Alkenes onto Carbon Surfaces: The Role of Photoelectron Ejection. *J. Am. Chem. Soc.* **2007**, *129*, 13554–13565.
36. Strother, T.; Knickerbocker, T.; Russell, J. N.; Butler, J. E.; Smith, L. M.; Hamers, R. J. Photochemical Functionalization of Diamond Films. *Langmuir* **2002**, *18*, 968–971.
37. Lu, M.; Knickerbocker, T.; Cai, W.; Yang, W.; Hamers, R. J.; Smith, L. M. Invasive Cleavage Reactions on DNA-Modified Diamond Surfaces. *Biopolymers* **2004**, *73*, 606–613.
38. Radadia, A. D.; Stavis, C. J.; Carr, R.; Zeng, H.; King, W. P.; Carlisle, J. A.; Aksimentiev, A.; Hamers, R. J.; Bashir, R. Control of Nanoscale Environment To Improve Stability of Immobilized Proteins on Diamond Surfaces. *Adv. Funct. Mater.* **2011**, *21*, 1040–1050.
39. Ozawa, M.; Inaguma, M.; Takahashi, M.; Kataoka, F.; Krueger, A.; Osawa, E. Preparation and Behavior of Brownish, Clear Nanodiamond Colloids. *Adv. Mater.* **2007**, *19*, 1201–1206.
40. Mochalin, V. N.; Shenderova, O.; Ho, D.; Gogotsi, Y. The Properties and Applications of Nanodiamonds. *Nat. Nanotechnol.* **2011**, *7*, 11–23.
41. Butler, J. E.; Sumant, A. V. The CVD of Nanodiamond Materials. *Chem. Vap. Deposition* **2008**, *14*, 145–160.
42. Orlando, A. Science and Technology of Ultrananocrystalline Diamond Film-Based MEMS and NEMS Devices and Systems. In *Ultrananocrystalline Diamond: Synthesis, Properties and Applications*; Shenderova, O. A., Gruen, D. M., Eds.; Elsevier Science: Amsterdam, 2012; pp 383–420.
43. Ralchenko, V.; Saveliev, A.; Voronina, S.; Dementjev, A.; Maslakov, K.; Salerno, M.; Podesta, A.; Milani, P. Nanodiamond Seeding for Nucleation and Growth of CVD Diamond Films. In *Proceedings of the NATO Advanced Research Workshop on Synthesis, Properties and Applications of Ultrananocrystalline Diamond*; Gruen, D. M., Shenderova, O. A., Vul', A. Y., Eds.; Springer: St. Petersburg, 2005; pp 109–124.
44. Affoune, A.; Prasad, B.; Sato, H.; Enoki, T. Electrophoretic Deposition of Nanosized Diamond Particles. *Langmuir* **2001**, *17*, 547–551.
45. Shenderova, O.; Hens, S.; McGuire, G. Seeding Slurries Based on Detonation Nanodiamond in DMSO. *Diamond Relat. Mater.* **2010**, *19*, 260–267.
46. Schmidlin, L.; Pichot, V.; Josset, S.; Pawlak, R.; Glatzel, T.; Kawai, S.; Meyer, E.; Spitzer, D. Two-Dimensional Nanodiamond Monolayers Deposited by Combined Ultracentrifugation and Electrophoresis Techniques. *Appl. Phys. Lett.* **2012**, *101*, 253111–253114.
47. Kim, J. H.; Lee, S. K.; Kwon, O. M.; Lim, D. S. Ultra Thin CVD Diamond Film Deposition by Electrostatic Self-Assembly Seeding Process with Nano-Diamond Particles. *J. Nanosci. Nanotechnol.* **2009**, *9*, 4121–4127.
48. Girard, H. A.; Perruchas, S.; Gesset, C.; Chaigneau, M.; Vieille, L.; Arnault, J. C.; Bergonzo, P.; Boilot, J. P.; Gacoin, T. Electrostatic Grafting of Diamond Nanoparticles: A Versatile Route to Nanocrystalline Diamond Thin Films. *ACS Appl. Mater. Interfaces* **2009**, *1*, 2738–2746.
49. Chen, Y.-C.; Tzeng, Y.; Cheng, A.-J.; Dean, R.; Park, M.; Wilamowski, B. M. Inkjet Printing of Nanodiamond Suspensions in Ethylene Glycol for CVD Growth of Patterned Diamond Structures and Practical Applications. *Diamond Relat. Mater.* **2009**, *18*, 146–150.
50. Zhuang, H.; Song, B.; Staedler, T.; Jiang, X. Microcontact Printing of Monodiamond Nanoparticles: An Effective Route to Patterned Diamond Structure Fabrication. *Langmuir* **2011**, *27*, 11981–11989.
51. Kondo, T.; Neitzel, I.; Mochalin, V. N.; Urai, J.; Yuasa, M.; Gogotsi, Y. Electrical Conductivity of Thermally Hydrogenated Nanodiamond Powders. *J. Appl. Phys.* **2013**, *113*, 214307–214311.
52. Varshney, M.; Li, Y. Interdigitated Array Microelectrodes Based Impedance Biosensors for Detection of Bacterial Cells. *Biosens. Bioelectron.* **2009**, *24*, 2951–2960.

53. Yang, L.; Li, Y.; Erf, G. F. Interdigitated Array Microelectrode-Based Electrochemical Impedance Immunosensor for Detection of *Escherichia coli* O157:H7. *Anal. Chem.* **2004**, *76*, 1107–1113.
54. Varshney, M.; Li, Y. Interdigitated Array Microelectrode based Impedance Biosensor Coupled with Magnetic Nanoparticle–Antibody Conjugates for Detection of *Escherichia coli* O157:H7 in Food Samples. *Biosens. Bioelectron.* **2007**, *22*, 2408–2414.
55. Sun, B.; Baker, S. E.; Butler, J. E.; Kim, H.; Russell, J. N.; Shang, L.; Tse, K.-Y.; Yang, W.; Hamers, R. J. Covalent Molecular Functionalization of Diamond Thin-Film Transistors. *Diamond Relat. Mater.* **2007**, *16*, 1608–1615.
56. Yang, W.; Butler, J. E.; Russell, J. N., Jr.; Hamers, R. J. Direct Electrical Detection of Antigen–Antibody Binding on Diamond and Silicon Substrates Using Electrical Impedance Spectroscopy. *Analyst* **2007**, *132*, 296–306.

Nanostructuring of Biosensing Electrodes with Nanodiamonds For Antibody Immobilization

Wenli Zhang[‡], Kush Patel[‡], Andrew Schexnider, Shirin Banu, Adarsh D. Radadia*.

Institute for Micromanufacturing, Center for Biomedical Engineering and Rehabilitation
Services, Louisiana Tech University, Ruston, LA 71272.

Supporting Information

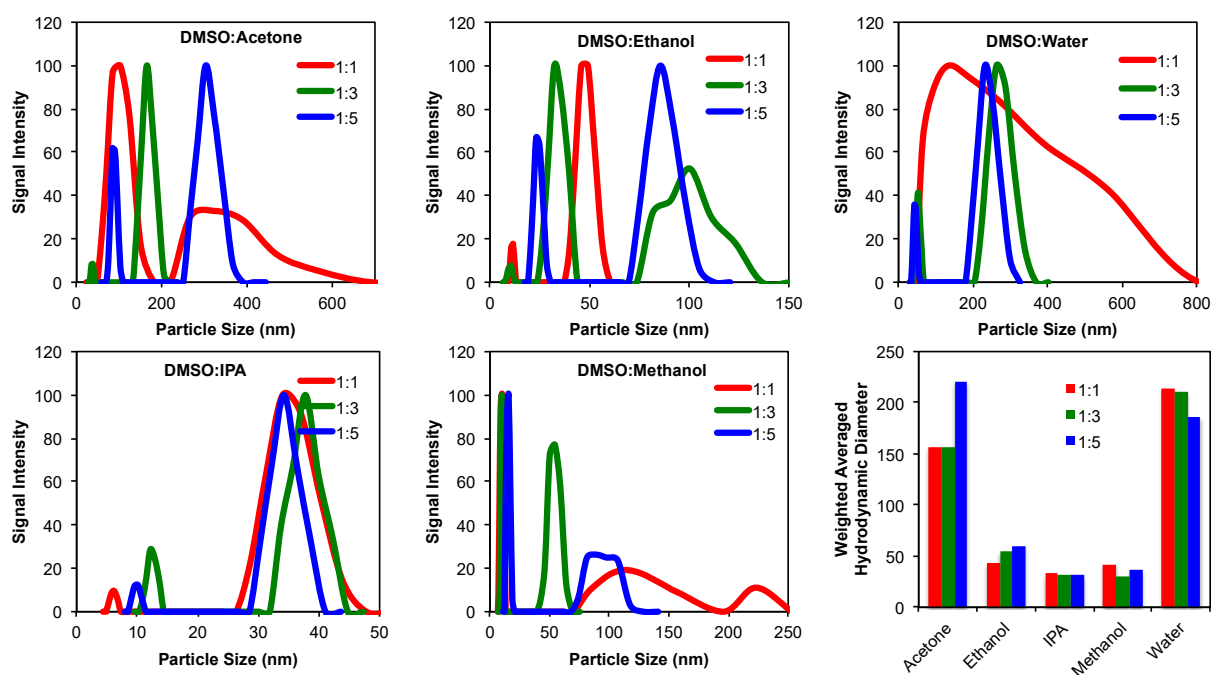


Figure S1. Results from photon correlation spectroscopy showing size distribution of ND aggregates obtained by diluting the original ND:DMSO solution with acetone, ethanol, water, IPA, and methanol.

Table S1. Properties of solvent mixtures estimated from molar ratio weighted calculations.

Solvent	Dilution Ratio	Molar Ratio	Dielectric Constant	Refractive Index	Density g/ml	Viscosity mPa-s
Acetone	1:1	0.4919	34.0572	1.4200	0.9390	0.5802
	1:3	0.7439	27.5817	1.3897	0.8625	0.4225
	1:5	0.8288	25.3997	1.3795	0.8370	0.3870
Ethanol	1:1	0.5506	34.5036	1.4140	0.9405	1.4465
	1:3	0.7861	29.2870	1.3862	0.8648	1.2705
	1:5	0.8597	27.6580	1.3776	0.8395	1.2239
IPA	1:1	0.4831	32.8357	1.4297	0.9385	2.2453
	1:3	0.7371	25.5455	1.4038	0.8618	2.3049
	1:5	0.8237	23.0594	1.3950	0.8362	2.3259
Methanol	1:1	0.6385	37.9524	1.3826	0.9415	0.8028
	1:3	0.8412	35.1749	1.3520	0.8663	0.6699
	1:5	0.8983	34.3934	1.3434	0.8412	0.6401
Water	1:1	0.7985	73.2897	1.3624	1.0450	1.1253
	1:3	0.9224	77.4161	1.3443	1.0215	1.0481
	1:5	0.9520	78.4000	1.3400	1.0137	1.0313

Table S1. Equivalent Circuit Fit Values For The Other Two Active Sensors.

Parameters	Active Sensor 2			Active Sensor 3		
	After antibody immobilization and blocking with casein	After capture from 10^6 cfu/ml	After capture from 10^8 cfu/ml	After antibody immobilization and blocking with casein	After capture from 10^6 cfu/ml	After capture from 10^8 cfu/ml
R1 (Ω)	13,591	9,148	8,269	21,655	13,498	10,105
R3 (Ω)	1,774	1,170	1,039	1,720	1,055	925
Ws1-R (Ω)	489,690	469,680	480,090	721,470	612,930	648,700
Ws1-T	5.02×10^{-3}			5.07×10^{-3}		
Ws1-P	0.7679			0.73527		
R2 (Ω)	25			25		
C1 (F)	2.75×10^{-9}			2.10×10^{-9}		
C2 (F)	1.46×10^{-9}			1.55×10^{-9}		

Table S2. Equivalent Circuit Fit Values For The Other Control Sensor.

Parameters	Control Sensor 2		
	After antibody immobilization and blocking with casein	After capture from 10^6 cfu/ml	After capture from 10^8 cfu/ml
R3 (Ω)	1,773	1,348	1,077
Ws1-R (Ω)	1.13×10^6	9.5×10^5	9.3×10^5
Ws1-T	8.6×10^{-3}		
Ws1-P	0.54		
R2 (Ω)	25		
C1 (F)	2.1×10^{-9}		
C2 (F)	1.3×10^{-9}		
R1 (Ω)	1×10^{-7}		